UCLA
UCLA Electronic Theses and Dissertations

Title
Understanding hardness of doped WB4.2

Permalink
https://escholarship.org/uc/item/2x40z9kx

Author
Shumilov, Kirill

Publication Date
2021

Peer reviewed|Thesis/dissertation

eScholarship.org Powered by the California Digital Library
University of California

UNIVERSITY OF CALIFORNIA
Los Angeles

Understanding hardness of doped $WB_{4.2}$

A thesis submitted in partial satisfaction
of the requirements for the degree
Master of Science in Chemistry

by

Kirill Shumilov

2021

© Copyright by
Kirill Shumilov
2021

ABSTRACT OF THE THESIS

Understanding hardness of doped $WB_{4.2}$

by

Kirill Shumilov
Master of Science in Chemistry
University of California, Los Angeles, 2021
Professor Anastassia N. Alexandrova, Chair

$WB_{4.2}$ is one of the hardest metals known. Though not harder than diamond and cubic boron nitride, it surpasses these established hard materials in being cheaper, easier to produce and process, and also more functional. Metal impurities have been shown to affect and in some cases further improve the intrinsic hardness of $WB_{4.2}$, but the mechanism of hardening remained elusive. In this work we first theoretically elucidate the preferred placements of Ti, V, Cr, Mn, Zr, Nb, Mo, Hf, Ta in the $WB_{4.2}$ structure, and show these metals to preferentially replace W in two competing positions with respect to the partially occupied B_3 cluster site. The impurities avoid the void position in the structure. Next, we analyze the chemical bonding within these identified doped structures, and propose two different mechanisms of strengthening the material, afforded by these impurities, and dependent on their nature. Smaller impurity atoms (Ti, V, Cr, Mn) with deeply lying valence atomic orbitals cause the inter-layer compression of $WB_{4.2}$, which strengthens the B_{hex}−$B_{cluster}$ bonding slightly. Larger impurities (Zr, Nb, Mo, Hf, Ta) with higher-energy valence orbitals, while expanding the structure and negatively impacting the B_{hex}−$B_{cluster}$ bonding, also form strong $B_{cluster}$−M bonds. The latter effect is an order of magnitude more substantial than the effect on the B_{hex}−$B_{cluster}$ bonding. We conclude that the effect of the impurities on the boride hardness does not simply reduce to structure interlocking due to the size difference between M and W, but instead, has a significant electronic origin.

The thesis of Kirill Shumilov is approved.

Sarah H. Tolbert

Richard B. Kaner

Anastassia N. Alexandrova, Committee Chair

University of California, Los Angeles

2021

TABLE OF CONTENTS

1 Introduction **1**

2 Computational Methods **4**

3 C, Si, and Zr **6**

3.1 The distribution of B_3-trimers 6

3.2 Bonding Analysis 8

3.3 Conclusion 11

4 Transition Metal Dopants **13**

4.1 Impurity Placement 13

4.2 Chemical Bonding 16

4.2.1 QTAIM 16

4.2.2 COHP and ICOHP 20

4.3 Conclusion 28

References **30**

LIST OF FIGURES

1.1 Structure of $WB_{4.2}$ 2

3.1 Properties of sampled $3 \times 2 \times 1$ supercell realizations 7

3.2 *Cmcm* model structure 8

3.3 QTAIM graphs of $WB_{4.2}$ dopped with C, Si, and Zr 10

3.4 Quantum Theory of Atoms and Molecules (QTAIM) analysis of bond critical points (BCPs) for C-, Si-, and Zr-dopped $WB_{4.2}$ 12

4.1 Model $WB_{4.2}$ $2 \times 2 \times 1$ supercell with single B_3 cluster. 14

4.2 Formation energy and volume of doped model structures 16

4.3 QTAIM graphs for the pure model structure 17

4.4 QTAIM analysis of *edge*-doped and *middle*-doped model structures 18

4.5 Bader charge analysis of *edge*-doped and *middle*-doped model structures . . . 19

4.6 ICOHP values of selected bonds in doped model structures 20

4.7 Bond distances of selected bonds in doped model structures 21

4.8 Atomic properties 23

4.9 B_{hex}−M bond COHP plots 25

4.10 B_{hex}−$B_{cluster}$ bond COHP plots 26

4.11 $B_{cluster}$−M bond COHP plots 27

LIST OF TABLES

3.1 Energies of formation, E_0, and bulk moduli, B_0, of model structures. 9

4.1 Distances between center of B_3-cluster and the metal impurity substituting W-atom in different positions in $WB_{4.2}$ $2 \times 2 \times 1$ supercell with single B_3. . . 13

ACKNOWLEDGMENTS

Adapted with permission from (Kirill D. Shumilov, Zerina Mehmedović, Hang Yin, Patricia Poths, Selbi Nuryyeva, Ieva Liepuoniute, Chelsea Jang, Isabelle Winardi, and Anastassia N. Alexandrova, "Understanding the Hardness of Doped WB4.2" *The Journal of Physical Chemistry C*, 2021, 125 (17), 9486-9496.) Copyright 2021 American Chemical Society.

CHAPTER 1

Introduction

Transition metal borides posses many of extremely useful mechanical properties such as high hardness, incomprehensibility, and temperature and wear resistance [TXZ12a, AYK17, GKS08, APM18]. A number of transition metal borides have Vicker's hardness greater than 40 GPa and bulk modulus larger than 300 GPa, which, coupled with their metallic nature and inexpensiveness, makes them excellent materials for superhard coating and cutting tools [CWL07b, CWL07a, MLX11, YLM16].

A vast number of superhard metal borides with various crystal structures has been discovered in recent years, including mono- [YLM16, LYM19], di- [LWZ19, CWL07b, CWL07a], tetra- [XMT15, MSZ11, MXL12, AYR18], and dodecaborides [ARS18, ASY16], as well as their solid solutions. It has been experimentally shown that the hardness of materials of this class can be controlled through *intrinsic*—originating from local chemical bonding—and *extrinsic*—resulting from surface grain boundaries and pattering—hardening effects. In this light, tungsten tetraboride stands out for its cost-effective synthesis and tunable hardness through addition of dopants [ARS18].

A number of transition metal impurities have been shown to enhance tungsten tetraboride's hardness and incomprehensibility intrinsically (Ti, Hf, Ta, Mo, etc.) and extrinsically (Zr, Y, Sc, Mn, etc.) [AYR18, XMT15, MTX16, MXL12, AYT16]. Despite ample experimental data, theoretical predictions of novel superhard tungsten tetraboride solid solutions has proven to be complicated. $WB_{4.2}$ posses a unique disordered crystal structure (Fig. 1.1A). It consists of alternating layers of hexagonal boron sheets (B_{hex}) and W atoms, with some of W substituted by B_3 clusters (2 clusters per 3 unit cells) [LTM15, KRF20]. The presence of B_3-trimers is crucial in the formation of the interlayer 3D-covalent boron-boron bonding network (so-called

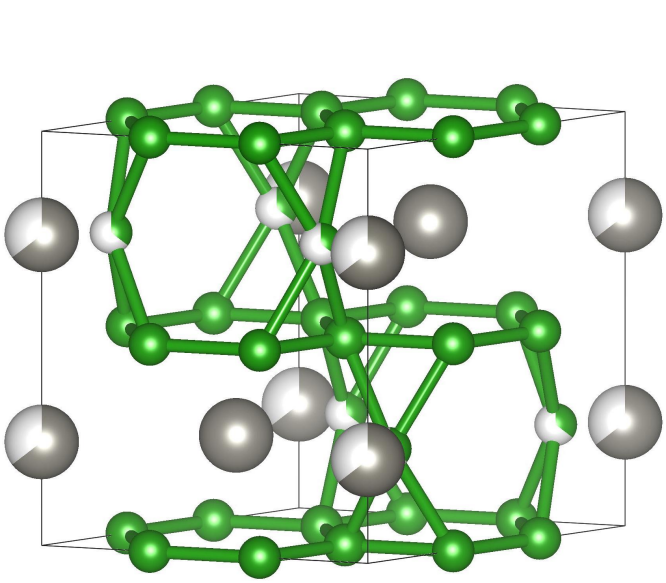

(A) $WB_{4.2}$ unit cell. Partially colored atoms indicate partial occupancy.

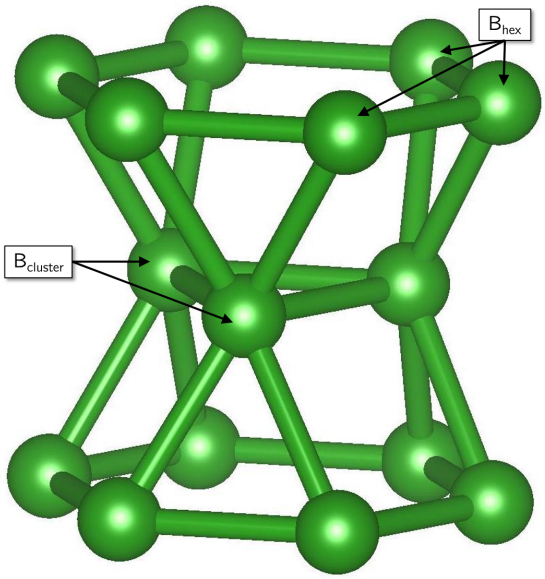

(B) Hourglass structure, formed by bonding between two hexagonal boron layers (B_{hex}) and B_3 cluster.

Figure 1.1: Structure of $WB_{4.2}$ with $P6_3/mmc$ space group, ICSD 291124. Boron atoms are colored in green, tungsten atoms are colored in gray; partially shaded atoms are partial occupancy sites that can be occupied by tungsten or B_3.

"hourglass" structures, Fig. 1.1B), which has been hypothesized to be responsible for the exceptional mechanical properties of the material, and particularly preventing the slip along the most "slippery" slip system [DLW19, GLS19]. However, the disorder embedded in the system presents a considerable challenge to pinpoint the bonding effects behind materials hardness, especially in the case of doped $WB_{4.2}$. Little is known about the preferred locations of various transition metal dopants in the tungsten tetraboride lattice, as well as their influence on the key hypothesized hardening element in this lattice—the hourglass structure. Understanding these structural and electronic effects of adding different transition metal impurities to the tetraboride is essential in the rational design of novel superhard materials.

In this work, we investigate effects of C, Si and transition metal impurities (Ti, Zr, Hf, V, Nb, Ta, Cr, Mo, and Mn) on the chemical bonding within a $WB_{4.2}$ model structure, containing a single B_3-trimer. Through the use of *ab initio* Density Functional Theory (DFT), coupled with Quantum Theory of Atoms and Molecules (QTAIM) and Crystal Orbital Hamiltonian Population (COHP) analysis, we study the preferred position of the impurity, as well as its qualitative and quantitative effect on the inter-layer bonding, in relation to material's hardness.

CHAPTER 2

Computational Methods

All calculations *ab initio* have been performed using the DFT Perdew-Burke-Ernzerhof (PBE) [PBE96, PBE97] Generalized Gradient Approximation (GGA) functional with the D3 [GAE10] dispersion correction, as implemented in Vienna *Ab-initio* Software Package (VASP) [KH93, KH94, KF96b, KF96a]. For this work we have decided to use PBE functional for all *ab initio* DFT computations. The functional is *de facto* standard for the majority of solid state calculations and became a power tool in investigating the $WB_{4.2}$ and its properties.[KRF20, DLW19, PWL18] Even though PBE has been known to underestimate mechanical properties of materials[RM15, ZRT18], it is sufficient enough for bonding analysis and is computationally easy to evaluate.

A 520 eV energy cutoff was used with $3 \times 3 \times 6$ Γ-centered Monkhorst-Pack k-points grid. Spin-polarized two-step geometry optimization was performed with 2^{nd} order Methfessel-Paxton smearing ($\sigma = 0.15$) for each structure until all atomic forces were $\leq 0.005\,\text{eV/Å}^2$. Each geometry optimization was followed by a static energy calculation using tetrahedron method with Blöchl corrections until the change in atomic energy was $\leq 1.0 \times 10^{-8}$ eV. We additionally performed the c-normal strain distortion calculations, by consecutive application of a $\varepsilon = 0.1$ engineered strain, starting from the ground state structure [TXZ12b]. Bulk modulus calculations were performed with the used of finite-difference method as implemented in VASP with expanded energy cutoff of 750 eV.

The sampling of potential geometric realizations of B_3-cluster distributions in $3 \times 2 \times 1$-supercell was performed with Site Occupancy Disorder (SOD) [GHC07]. DFT calculations were used to narrow the space of search. A subset of output structures were chosen, including but not limited to, structures of high symmetry, high bulk modulus, low energy, etc.

QTAIM calculations were performed using the `Critic2` [RBP09, RJL14] software. Electron density for QTAIM calculations was obtained from special static VASP calculations with double the number of grid points in the FFT-grid. Identification of critical points was based on recursive subdivision of the Wigner-Seitz cell algorithm. Atomic basin interactions to calculate atomic Bader charges utilized Yu and Trinkle (YT) [YT11] method.

ICOHP calculations have been performed using the `Lobster` [DTD11, MDT13, MDT16, NEG20] package. Wavefunctions for ICOHP were taken from special static VASP calculations with twice as many bands as normal calculations. `pbeVaspFit2015` [MDT16] basis set was used to achieve $\leq 1.8\,\%$ average absolute charge spilling.

CHAPTER 3

C, Si, and Zr

3.1 The distribution of B_3-trimers

The $WB_{4.2}$ unit cell structure with $P6_3/mmc$ space group symmetry was used in this Chapter (Fig. 4.1A). However, as it was the crystal structure of $WB_{4.2}$ is disordered with $\sim 2/3$ chance of B_3-trimer substituting a W-atom in Wyckoff 2(b) position. Therefore, to account for fractional occupancy sites, a $3 \times 2 \times 1$-supercell was chosen, since it is the smallest supercell that guarantees an integer number—four—of B_3-trimers in the structure. Within this supercell, a set of structures was sampled, including but not limited to, structures of high symmetry, high bulk modulus, low energy, etc. (Fig. 3.1). The $Cmcm$ structure (Fig. 3.2) is the one on which we focus the discussion. Not only it is a structure with the highest symmetry $Cmcm$, but also with the highest bulk modulus ($B_0 = \sim 293\,\text{GPa}$.) Furthermore, $Cmcm$ structure was found to be the most stable under at finite temperature with inclusion of configurational entropy [GLS19].

Additionally, the bulk moduli were calculated for variation of impurity and position (Table 3.1). The values of bulk moduli obtained from *ab initio* methods significantly underestimate the experimental results. The discrepancy can be primarily attributed to the use of insufficient level of theory (PBE functionals), poor treatment of Van der Waals interactions (vdW), and disregard for relativistic effects in W atoms. It has been shown that PBE functionals tend to noticeably delocalize electrons and, as a result, underestimate the bulk modulus by approximately 8.9% [RM15]. We have attempted to recalculated the bulk modulus for pure and C-doped structures with HSE06 hybrid functionals [HSE03, HSE06], since this higher level of theory features greater electron localization and can also correct

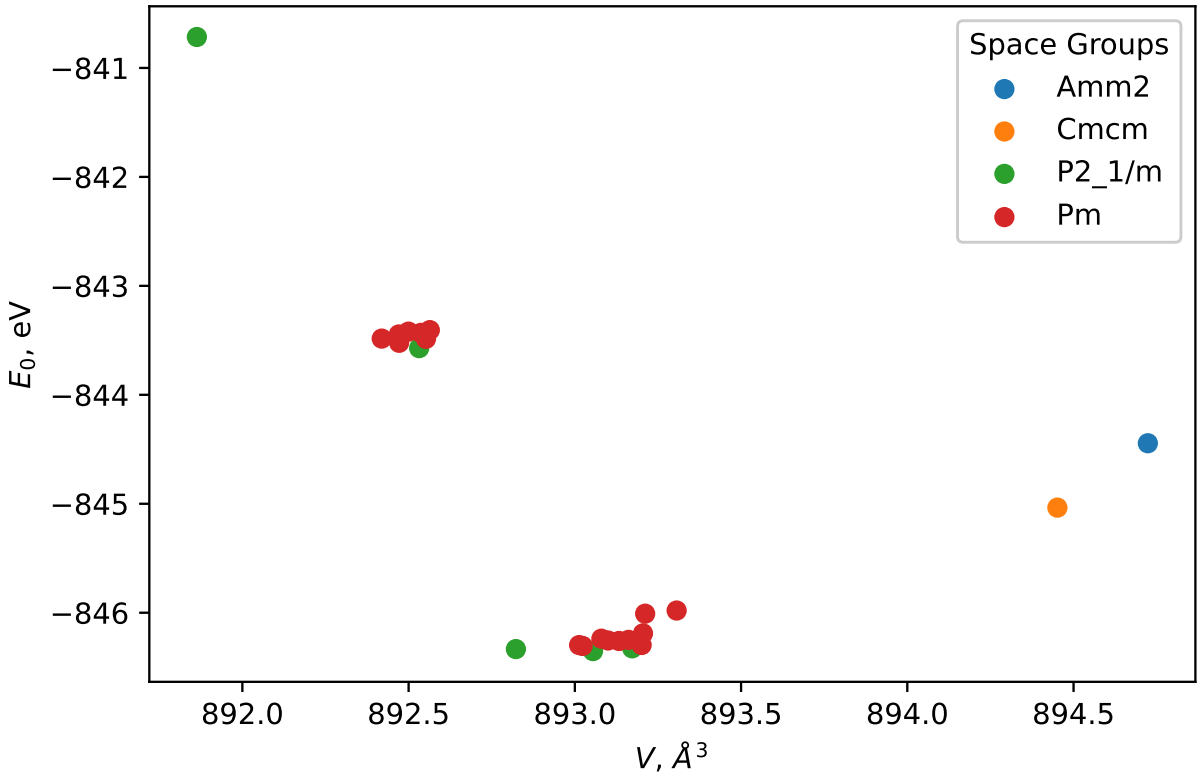

Figure 3.1: Energies (E_0) and volumes (V) of sampled realizations of $3 \times 2 \times 1$ $WB_{4.2}$ supercell

potential vdW issues. Even though we have observed an increase in bulk moduli of these structures, the change was still insufficient to match the experimental result. However, the relative difference between bulk moduli of pure and C-doped structures, when calculated with HSE06 and PBE, has not changed significantly, indicative of reliable trend between these structures. Furthermore, the QTAIM graphs remained qualitatively the same for HSE06 and PBE. Possibly an appropriate *ab initio* methods treating strong electron correlation could aid in correctly estimating the bulk modulus of $WB_{4.2}$, but those methods are inaccessible for solid state calculations. Therefore, PBE functional has been chosen for future calculations due to its relative computational efficiency, despite the better estimates of bulk modulus obtained with HSE06. The inclusion of Si decreases the computed bulk modulus, B_0, while the inclusion of C leaves the computed B_0 practically unchanged. The introduction of Zr in either position marginally increases B_0.

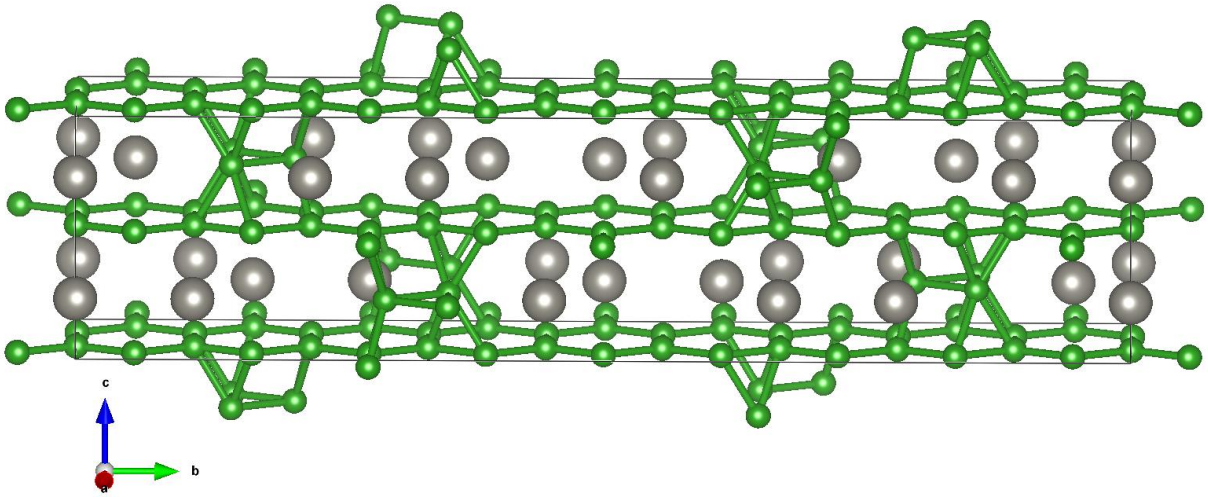

Figure 3.2: Model structure with *Cmcm* symmetry. A characteristic feature of this structure is alternating "rows" of B_3-trimers, "piercing" the material along the $\vec{a}$-axis.

3.2 Bonding Analysis

Since chemical bonding is local and largely covalent in this material, we created a smaller model, a $2 \times 2 \times 1$-supercell with a single B_3-trimer, isolated from other trimers (Fig. 4.1A). To analyze the local bonding of the impurities, we used QTAIM, a Quantum Theory of Atoms and Molecules, a mathematically rigorous formalism to analyze the properties of the electron density, and connect those to chemical properties. The eigenvalues of the Hessians of *critical points (CPs)* in the charge density—points where all three first derivative of the density with respect to spatial coordinates vanish—reveal the bonding information. There are 4 types of critical points in three-dimensional space: nuclear critical point (NCP) with all three Hessian eigenvalues positive, bond critical point (BCP)—two eigenvalues positive, ring critical point (RCP)—two eigenvalues negative, cage critical point (CCP) with all three Hessian eigenvalues negative. In this Chapter, we primarily focus on BCPs and their properties. Each BCP

Impurity	Position	B_0, GPa	E_0, eV
Pure material	N/A	292.7	−12.6
C	Two B atoms in B_{hex}-layer above B_3-trimers	292.1	−8.7
	Four B atoms in B_{hex}-layer above B_3-trimers	289.8	−5.1
	One B atom in B_3-trimer	288.6	−7.3
Si	Two B atoms in B_{hex}-layer above B_3-trimer	274.9	−6.9
	One B atom in B_3-trimer	280.5	−9.2
	B_3-trimer	281.7	−10.4
Zr	W-occupancy	295.3	−12.9
	W-vacancy	292.0	−12.8

Table 3.1: Energies of formation, E_0, and bulk moduli, B_0, of model structures.

is connected via *bond paths* to two NCPs, associated with two different nuclei in the cell. Two properties are commonly used to qualitatively compare BCPs: the electron density (ρ) and the Laplacian of the electron density ($\nabla^2\rho$). A stronger bond would generally have a high electron density and a more negative Laplacian at its BCP, while a weaker bond would generally have a smaller electron density and a more positive Laplacian. The relevant QTAIM graphs are shown in the Fig. 3.3.

Due to the pseudo-layered nature of the material, the weakest slip system in $WB_{4.2}$ is the shear in the [001] plane. Therefore, the bonds connecting hexagonal layers either through B_3-trimers or through metal atoms are essential for strengthening $WB_{4.2}$ against shear. The strongest bond formed in the C-doped $WB_{4.2}$ is the 2-center bond between B in B_3-trimer and C in the B_{hex}-layer (Fig. 3.4). It has the highest electron density and lowest Laplacian in the entire structure. The formation of the strong C_{hex}−$B_{cluster}$ bond is likely related to the resistance of the material to shear. The bonds formed with other impurities generally have lower electron density and high positive Laplacian, associated with bond weakening. For instance, the substitution of W with Zr instead of W in Wychoff 2c leaves the interlayer

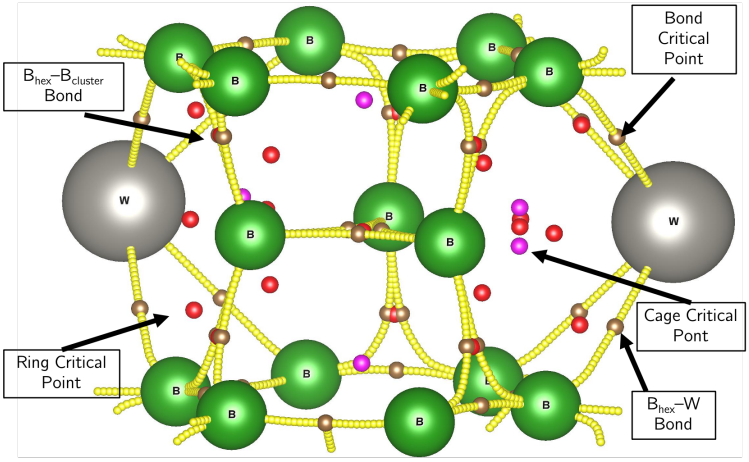

(A) Pure $WB_{4.2}$

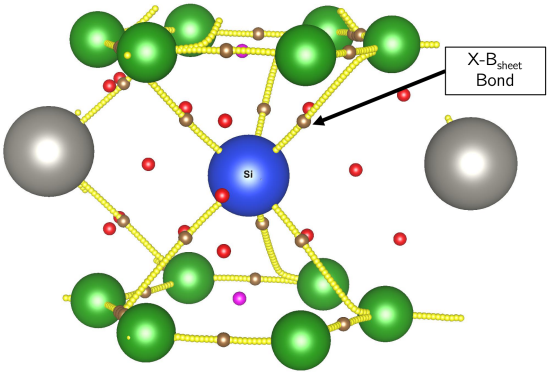

(B) Si substitutes B_3-trimer

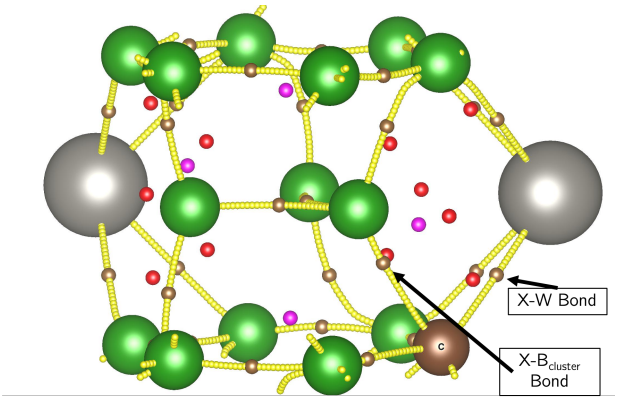

(C) C in B_{sheet}

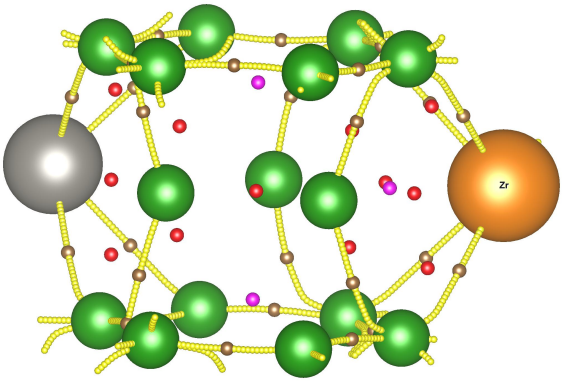

(D) Zr in W-occupied Wyckoff $2(c)$

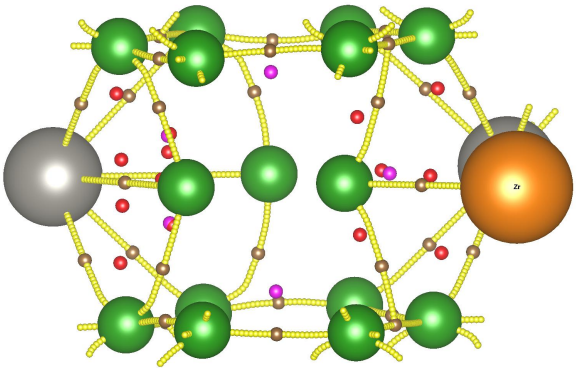

(E) Zr in unoccupied Wyckoff $2(d)$

Figure 3.3: Bonding QTAIM analysis of model structures with selected impurities. Point descriptions: Bond CPs — brown, Ring CPs — red, Cage CPs — magenta. Lines of gold critical points depict bond paths.

bonding unchanged or weakens it, while substitution of Zr in W-vacancy always depletes the electron density of interlayer bonds. An extreme example of bond weaking is Si, upon substituting the entire B_3-cluster. The bonds it forms with the B_{hex} are characterized by small $\rho(\vec{r})$ and near-zero $\nabla\rho(\vec{r})$). While the metal dopants generally slightly weaken B_{hex}−$B_{cluster}$ (lower in $\rho(\vec{r})$ and higher in $\nabla\rho(\vec{r})$), the Si impurity replaces those bonds with significantly weaker bonds.

3.3 Conclusion

In this chapter we sampled possible realizations of $WB_{4.2}$ $3 \times 2 \times 1$ supercell, identified viable positions of the impurity placement and its effect on bulk modulus of the material, and studied bonds formed by the C, Si, and Zr impurities, employing QTAIM analysis. Our investigation of ensemble of possible structure realizations in combination with bulk modulus calculations, despite their divergence from experimental values, allowed us to confirm the validity of chosen level of theory. Furthermore, based on the aforementioned results, we were able select small model structure ($2 \times 2 \times 1$ supercell with single B_3-cluster,) reproducing the bonding character of the material.

Applying QTAIM analysis to the model structure, we showed that the C impurity, when placed in the hexagonal sheet near the B_3-trimer, generally forms the strongest interlayer C_{hex}−$B_{cluster}$ bonds, in place of B_{hex}−$B_{cluster}$. Other impurities tend to form interlayer bonds that either weaker than B_{hex}−$B_{cluster}$, as in the case of Si, or as strong as B_{hex}−W, as in the case of Zr. As a result, we expect C-dopped $WB_{4.2}$ to be harder and Si-dopped $WB_{4.2}$ to be softer than pure $WB_{4.2}$. The bonding effect of the Zr impurity, as seen in the QTAIM analysis, is not pronounced enough and requires further study. The $2 \times 2 \times 1$ supercell structure with a single B_3-trimer was shown to be a convenient model for understanding crucial interactions between hexagonal B-sheets, W-atoms, B_3-clusters, and impurities. As a result, it is used further in combination with COHP and QTAIM analyses to closely research transition metal doping in $WB_{4.2}$.

(A) Average Bader charges in model structures.

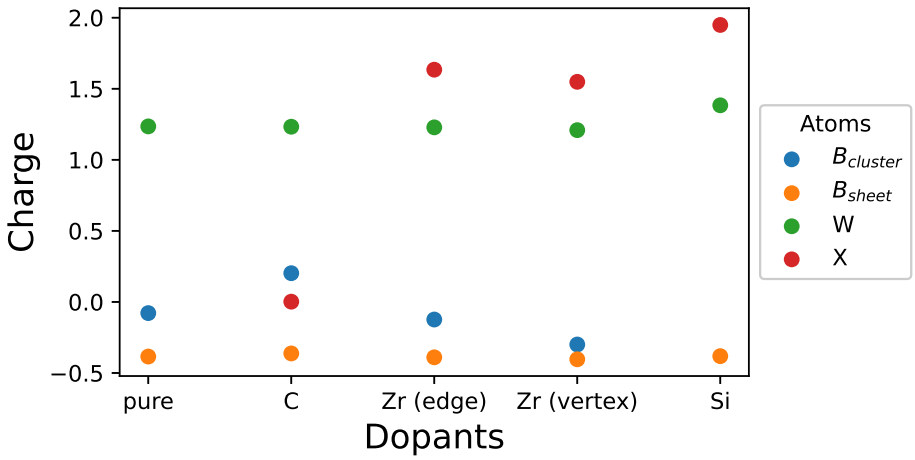

(B) Average electron density at BCPs, connecting "layers" of material.

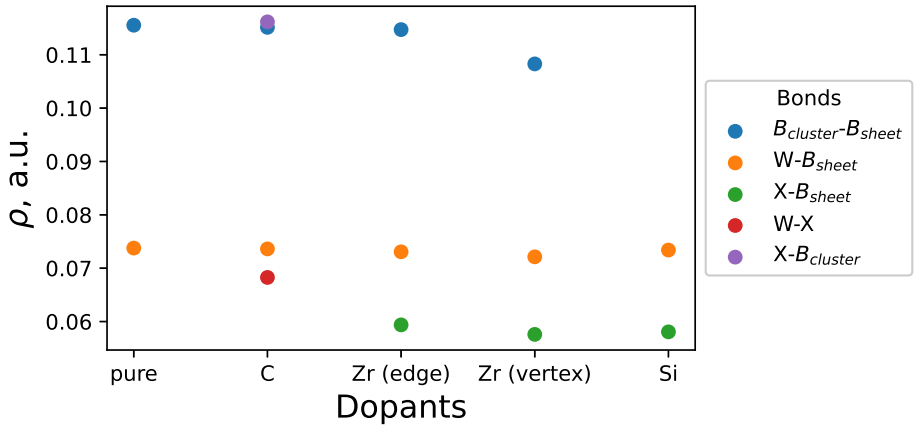

(C) Average Laplacian at BCPs, connecting "layers" of material.

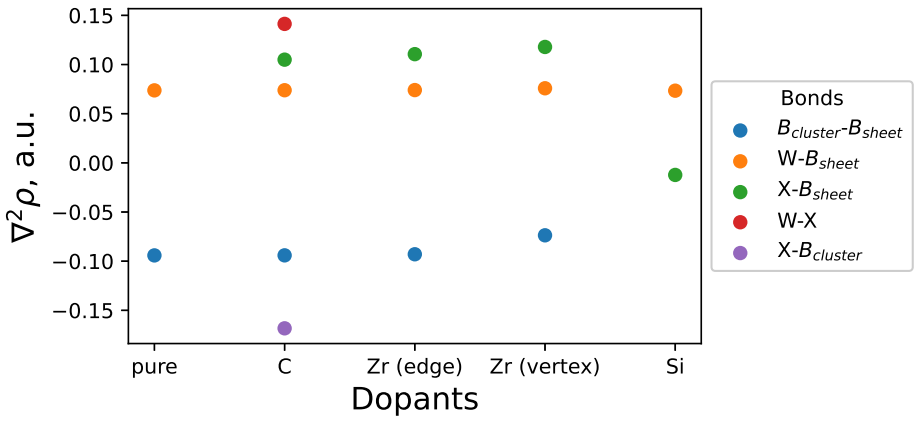

Figure 3.4: QTAIM analysis of BCPs for model structures.

CHAPTER 4

Transition Metal Dopants

4.1 Impurity Placement

A simple $WB_{4.2}$ $2 \times 2 \times 1$ supercell with a single B_3-trimer (221.1B3) substituting one of W (Fig. 4.1A) has been chosen to carry out the majority of calculations. Despite the non-experimental ratio of B to W (one B_3-trimer per four unit cells, instead of four B_3-trimers per six unit cells) this model was more affordable, and allowed us to explore more extensively the position of the impurity, while did not prevent understanding the local bonding effects of (M) within the material.

We began our search by investigating the various positions that M can occupy. Based on our model structure, the impurity can occupy one of only five unique positions, substituting W at various distances with respect to the B_3 cluster, listed in Table 4.1 and shown in Fig. 4.1.

Table 4.1: Distances between center of B_3-cluster and the metal impurity substituting W-atom in different positions in $WB_{4.2}$ $2 \times 2 \times 1$ supercell with single B_3.

Position	Distance, Å	Layer	Impurity Type
Vertex	2.96	Same as B_3-cluster	Interstitial (inserts into W void)
Edge	2.96		Substitutes W
Middle	5.17		
Far	5.97		
Top	3.15	Different layer	

Structures with impurities at different positions were geometrically optimized and their

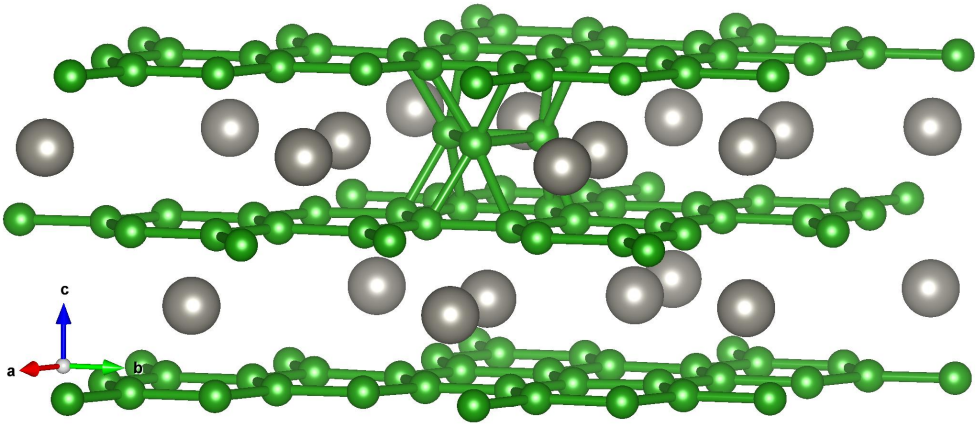

(A) Pure (a.k.a. 221.1B3), $B_{51}W_{15}$

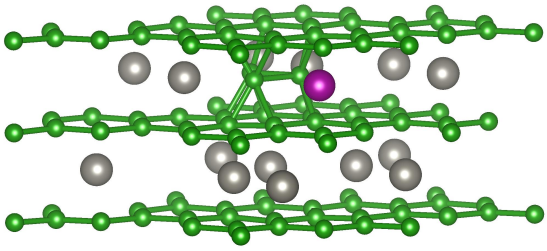

(B) *Edge*-doped, $M_1B_{51}W_{14}$

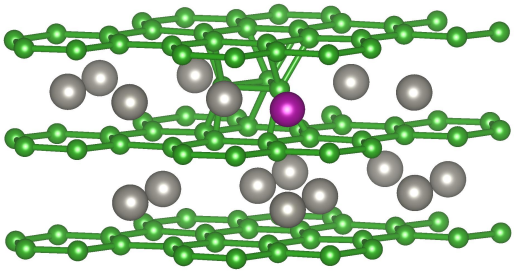

(C) *Middle*-doped, $M_1B_{51}W_{14}$

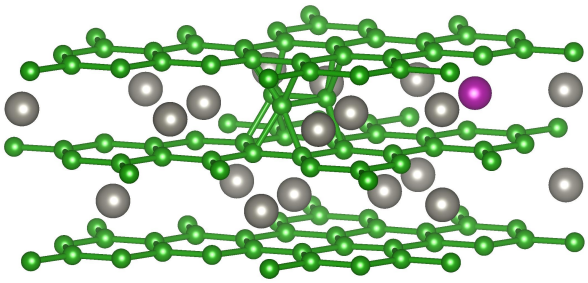

(D) *Far*-doped, $M_1B_{51}W_{14}$

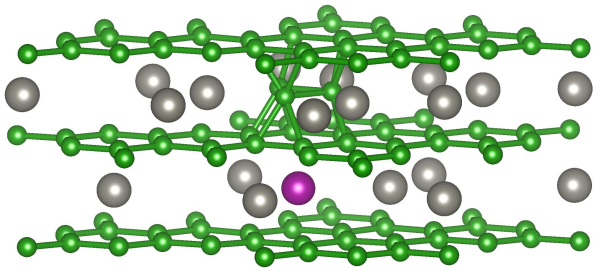

(E) *Top*-doped, $M_1B_{51}W_{14}$

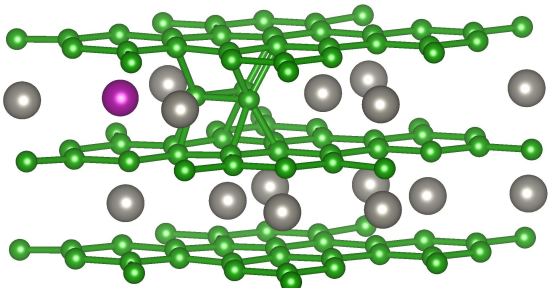

(F) *Vertex*-doped, $M_1B_{51}W_{15}$

Figure 4.1: Model $WB_{4.2}$ $2 \times 2 \times 1$ supercell with single B_3 cluster.

energies of formation from the pure bulk boron and bulk metals were calculated for each structure (Fig. 4.2). Despite the lack of the zero-point energy corrections to the energies, the calculated energies of formation combined with the volume information clearly indicated the presence of strong bonding changes, occurring with the addition of the impurity. The volume change (Fig. 4.2B) shows strong dependence on the atomic radius of the impurity, regardless of the position of the impurity. Indeed, it can be noticed that generally fourth row elements, possessing smaller atomic radii, cause contraction of the structure, while larger elements, such as Zr and Hf, cause the cell to expand. The change in volume occurs mostly through elongation or shortening along the *c*-axis, or, in other words, through distance change between the hexagonal boron sheets, relative to the initial model structure (Fig. 4.1A). Notice that *vertex*-doped structures (i.e. structures where the impurity occupies the void in the lattice) are generally associated with larger volumes and energies of formation, relative to the initial model structure. This observation suggests that placing the dopant in the void of the parent boride is considerably unfavorable. For this reason, we do not focus on the *vertex*-doped structures in the rest of the paper, though include the computed properties for these structures, for completeness. For all other positions, we see that almost all dopants (except Cr and Mn) have smaller ΔE_f than that of 221.1B3. The lack of clear correlation between the energy of formation and atomic size of the impurity points to the presence of additional chemical bonding effects in the cases of substitutional doping. Interestingly, the alteration in the position of the impurity for substitutional doping does not change the volume, or the energy of formation significantly (overall variation between positions for a single dopant is $\leq 2.0\,\text{eV}$).

Due to the lack of differentiation based on ΔE_f between the substitutional impurities in different positions, we now focus on the specifics of the electronic structure in both the *edge* and the *middle* configurations. These positions are additionally chosen such that the interaction between the cluster and the impurity is substantial, since the clusters have been hypothesized to contribute to the boride hardness. The *edge* position is especially interesting due to its proximity to the B_3 cluster, suggesting the biggest impact on its bonding.

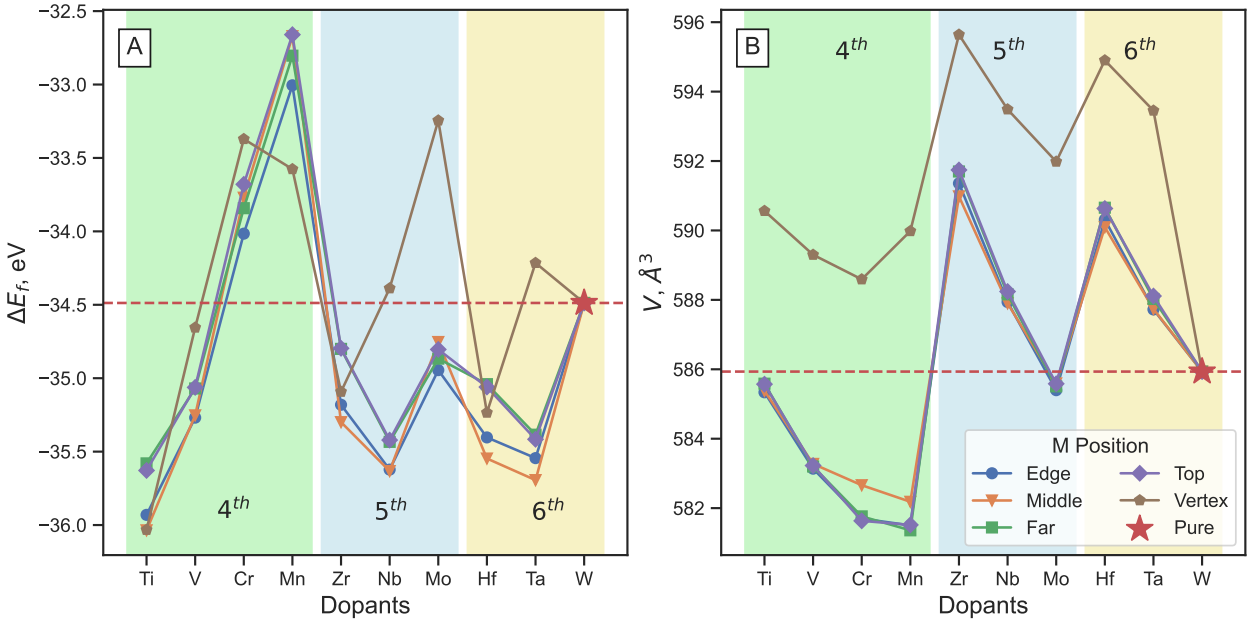

Figure 4.2: Formation energy (A) and volume (B) of doped model structures. The shade of the background indicates the period of the dopant.

4.2 Chemical Bonding

4.2.1 QTAIM

To explore the underlying chemical bonding effects, and particularly the nature of the interactions between M, W, B_3, and hexagonal boron layers, we first employ QTAIM.

Relevant QTAIM graphs for model structures are shown in Fig. 4.3. The QTAIM graphs of model structures with impurities did not differ significantly in the geometry of critical points and, thus, are not shown. The properties of BCPs (B_{hex}–$B_{cluster}$, B_{hex}–W, B_{hex}–M), connecting boron hexagonal layers, are shown in the Fig. 4.4. Bader charges calculated for the B_3-trimers and W atoms are shown in Fig. 4.5.

From Fig. 4.4 A1,B1, as well as Fig. 4.5, one can see the similar "climbing zig-zag" trend as the one observed in the changes of the volume (Fig. 4.2.) The trend is better visible in the cases of *edge*-doped structures, especially in such BCP properties as ρ and the Bader charge. The trend is less noticeable for $\nabla^2\rho$. The "climbing zip-zag" pattern could be linked to the atomic radius of the impurity and its proximity to the cluster. We see that the smaller

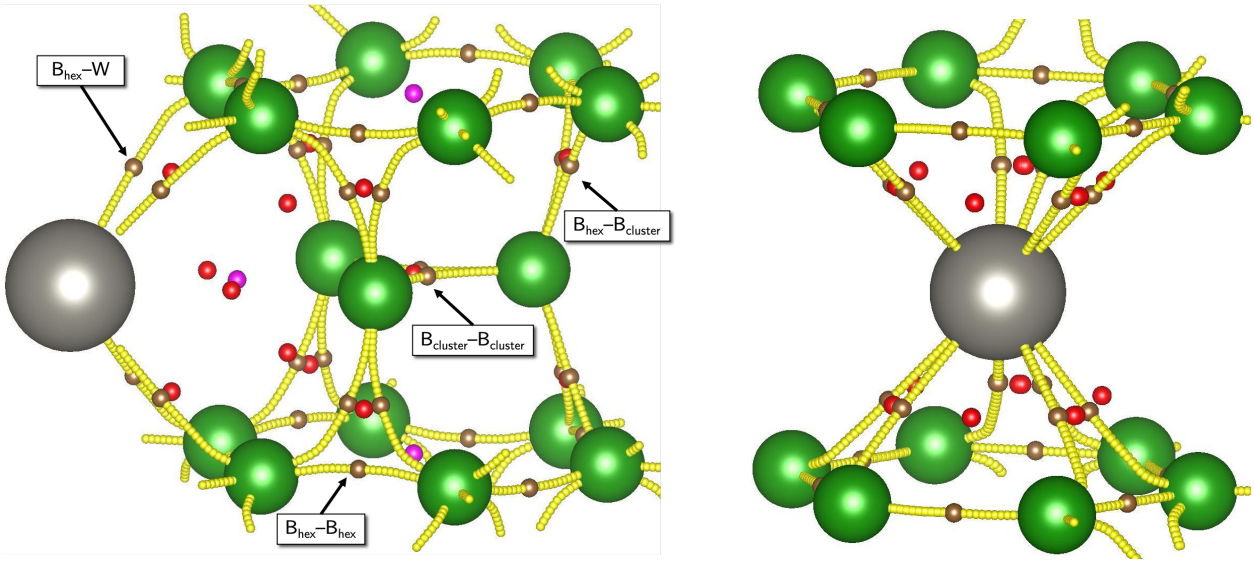

(A) Example of QTAIM bond paths within the hourglass structure. Only one W atom out of three is shown for clarity.

(B) Example of QTAIM bond paths around the W atom.

Figure 4.3: QTAIM plots for the pure model structure. BCP points are colored in brown, RCP—in red, CCP—in magenta. Bond paths are shown in sequences of yellow points.

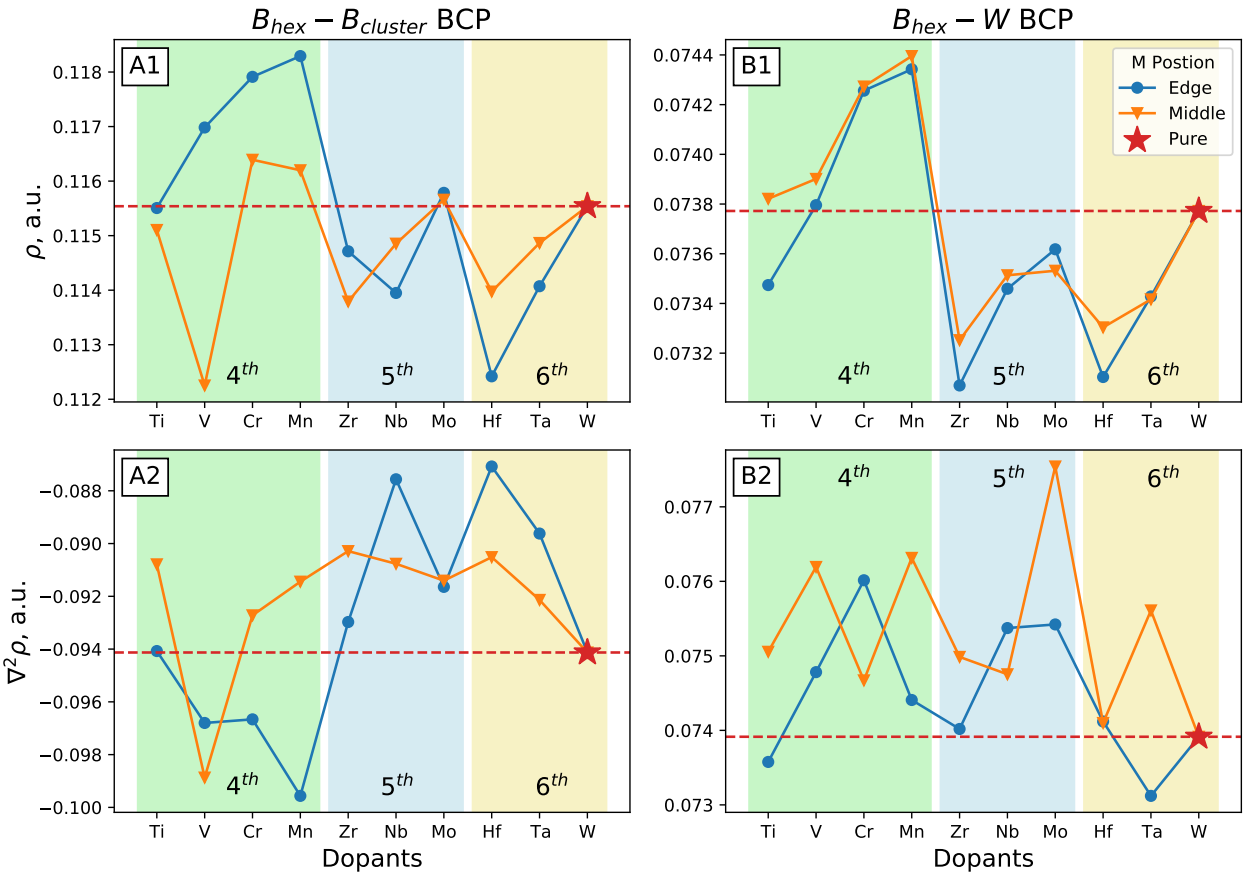

Figure 4.4: QTAIM analysis of *edge*-doped and *middle*-doped model structures. (A1) Average electron density and (A2) Laplacian at B_{hex}–$B_{cluster}$ BCP. (B1) Average electron density and (B2) Laplacian at B_{hex}–W BCP.

impurities are generally associated with larger ρ at the inter-layer BCPs and more negative $\nabla^2\rho$, as well as more positively charged B_3 and more negatively charged impurity. The shorter distances of the impurity to the cluster strengthen the effects of the smaller atomic radii, and larger distances weaken them.

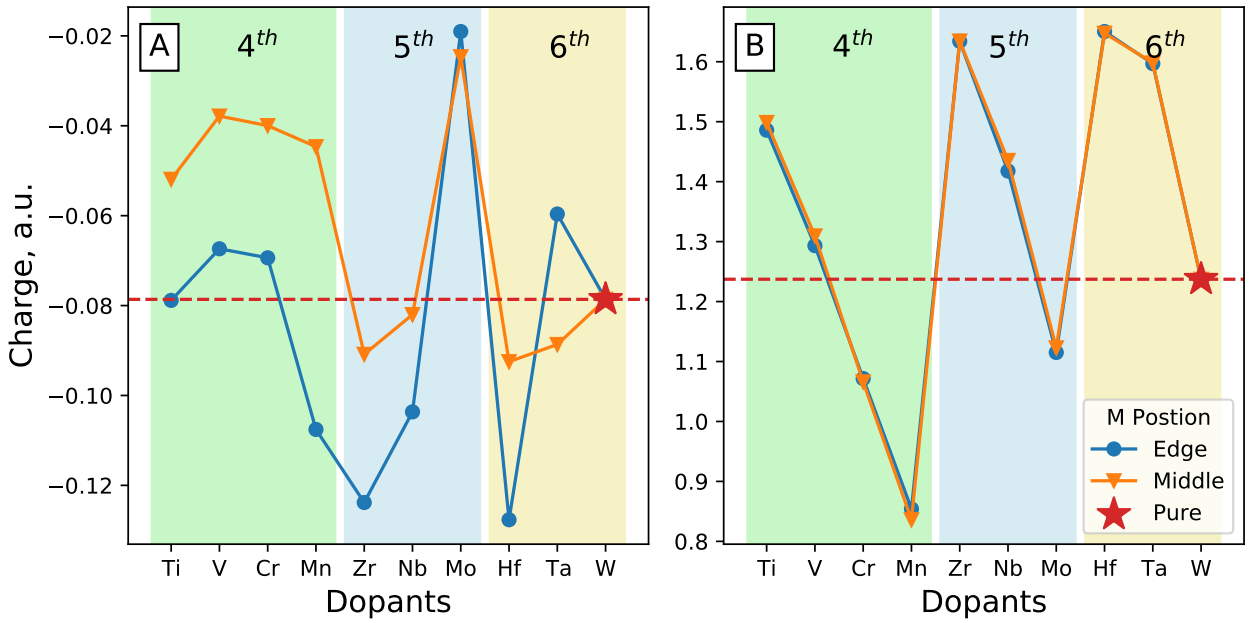

Figure 4.5: QTAIM analysis of *edge*-doped and *middle*-doped model structures. (A) Total Bader charge on the B_3-cluster. (B) Average Bader charge on W atoms.

However, for the purposes of this study, QTAIM analysis is insufficient, because it does not directly provide energetic information, and therefore, allows for only qualitative comparisons between different types of bonds, or relative to some "standard." Furthermore, CP evaluation in QTAIM relies on the integration and differentiation of electron density, implemented on a grid for periodic systems, and therefore bearing some inaccuracy, especially when CP are proximal. $WB_{4.2}$ is prone to such errors. As we can see from small negative $\nabla^2\rho$ (Fig. 4.4), a great number of bonds in the system are electron-deficient, resulting in very curved bond paths (Fig. 4.3). The CPs defining these paths appear to "merge" into a single CP for some systems, due to their proximity and the insufficient resolution of the electron density grid. Thus, we use QTAIM only to guide our search for the bonding mechanism in $WB_{4.2}$, but not for the evaluation of the relative strengths of the key bonding effects.

4.2.2 COHP and ICOHP

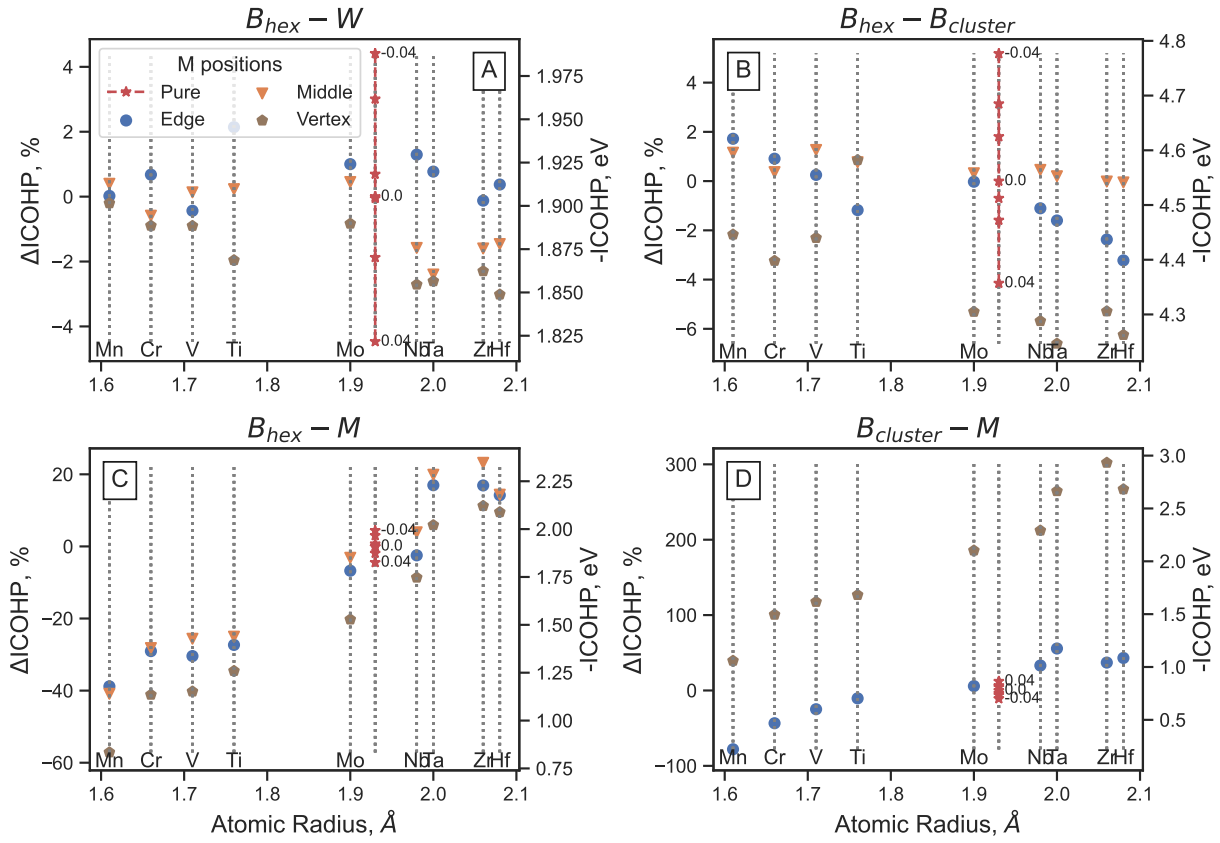

Figure 4.6: Comparison of the pure *c*-strained model structure (red, with the stress values labeled), the *edge*-doped (blue), *middle*-doped (orange), and *vertex*-doped model structures. Average bond ICOHP of (A) B_{hex}−W bond, (B) $B_{cluster}$−W bond, (C) B_{hex}−B_M bond, and (D) $B_{cluster}$−M bond as a function of the atomic calculated radius[CRR67] of the impurity metal. The numbers next the *pure* line indicate the engineered strain, applied along the *c*-axis of pure model structure. Left *y*-scale indicates ΔICOHP as defined by Eq. 4.1 and right *y*-scale indicates absolute value of −ICOHP.

COHP analysis was done to assign energetics to the bonds found by QTAIM. COHP analysis works by partitioning the band structure of a crystal into pair-wise energy-weighted orbital interactions. By integrating COHP up to the Fermi level, one can obtain a good estimation of a bond strength in a solid-state. More negative ICOHP values are associated with stronger bonds, and vice-versa. By averaging ICOHP over bonds identified by QTAIM,

we can estimate the changes in stability upon addition of an impurity.

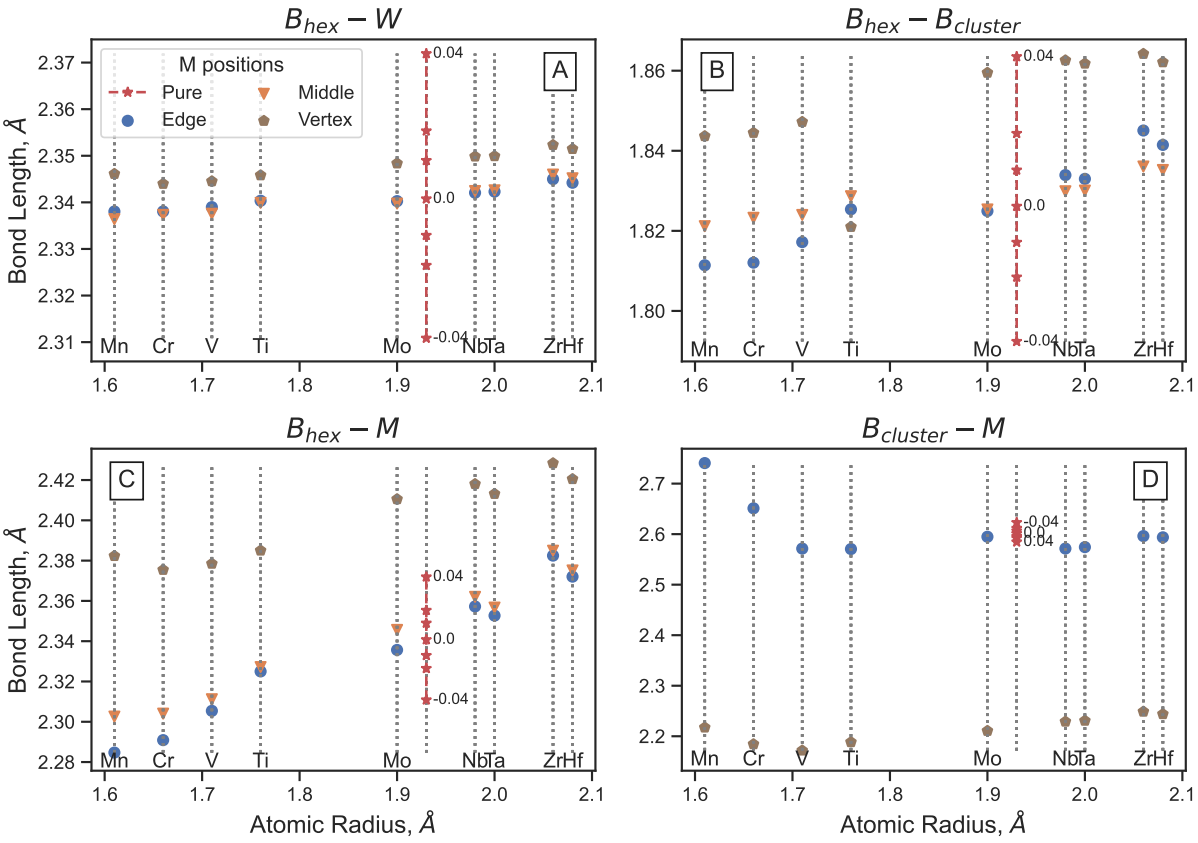

Figure 4.7: Comparison of the pure *c*-strained model structure, *edge*-doped, *middle*-doped, and *vertex*-doped model structures. The average bond length of (A) B_{hex}−W bond, (B) $B_{cluster}$−W bond, (C) B_{hex}−B_M bond, and (D) $B_{cluster}$−M bond, as a function of the calculated atomic radius[CRR67] of the impurity. The numbers next the *pure* line indicate the engineered strain, applied along the *c*-axis of pure model structure.

Here, we aim to deconvolute the effect of the size of the impurity atom from the additional bonding effects that the impurity brings. Therefore, as a purely theoretical reference, we applied a set of normal strains ($\epsilon \in [-0.04, -0.02, -0.01, 0.01, 0.02, 0.04]$) along the *c*-axis of the pure model structure, to mimic the incorporation of the impurities of all sizes, from small to large, but without additional electronic effects. We relaxed all degrees of freedom in the strained structures, and calculated ICOHP (vertical red lines in Fig. 4.6 and Fig. 4.7). For *edge*-, *middle*-, and *vertex*-doped structures the analogous analysis was performed (Fig. 4.6

and Fig. 4.7). The y-axis in Fig. 4.6, is calculated according to the formula:

$$\Delta\text{ICOHP}_i = \frac{\text{ICOHP}_i - \text{ICOHP}_{\text{pure}}}{\text{ICOHP}_{\text{pure}}} \tag{4.1}$$

Vertex-doped structures was included in the COHP and ICOHP calculation to further prove that interstitial doping is unfavorable and leads to destabilization. In the Fig. 4.6, we, indeed, see that generally *vertex*-positioned impurities cause decrease in the strength of all inter-layer bonds, as compared to pure and *edge*-, *middle*-doped structures.

For the case of substitutional doping, we can see that on average the strongest inter-layer bond is B_{hex}−$B_{cluster}$, followed by B_{hex}−W and B_{hex}−M of competitive strengths. Firstly, the addition of an impurity in any position has little effect on the strength and length of the B_{hex}−W bonds (Fig. 4.7A), suggesting that the equilibrium inter-layer separation in the boride is defined by that bond length. On the other hand, the strongest bond, B_{hex}−$B_{cluster}$, is sensitive to the nature and position of the impurity. While it experiences a rather little change in ICOHP in the case of the *middle* doping, a significant change is seen in the case of the *edge* doping. Moreover, the impurities can be classified as two types: the 4^{th} period elements (Ti, V, Cr, Mn), and the later period elements. Both types quite linearly affect the B_{hex}−$B_{cluster}$ distance and bond strength as functions of the atomic radius of the impurity, though to a slightly different degree. As the impurity atoms gets larger, the cluster-layer boron bonding weakens. Therefore, the boron-boron bonding in the parent tetraboride appears to be slightly compromised by the large size of the W atom, which adds a strain to the structure by separating the boron layers and clusters more than their equilibrium distance would be without W in the lattice.

The biggest difference is seen in the B_{hex}−M bonds. Contrary to the B_{hex}−$B_{cluster}$ bond, the B_{hex}−M bond is stronger for the latter period impurities in the *edge* and *middle* positions. Note that the bond strength change is more dramatic than for the B_{hex}−$B_{cluster}$ bonds, and constitutes the most significant electronic structure impact of the impurity on the boride. To summarize, we see that the 4^{th} period elements strengthen the B_{hex}−$B_{cluster}$ bonds by bringing the clusters and layers of boron closer together and apparently enhancing the covalent bonding overlap (presumably therefore strained by the larger W atoms in the undoped boride). On

the contrary, the 5$^{\text{th}}$ and 6$^{\text{th}}$ period elements increase the boron cluster-layer separation and adversely affect the bonding there, but are capable of strong B_{hex}−M bonding interactions that counterbalance the effect (Fig. 4.7.) In addition, we observe the $B_{cluster}$−M bond in some cases, which is overall very weak, though marginally stronger for the latter period elements, as will be shown shortly.

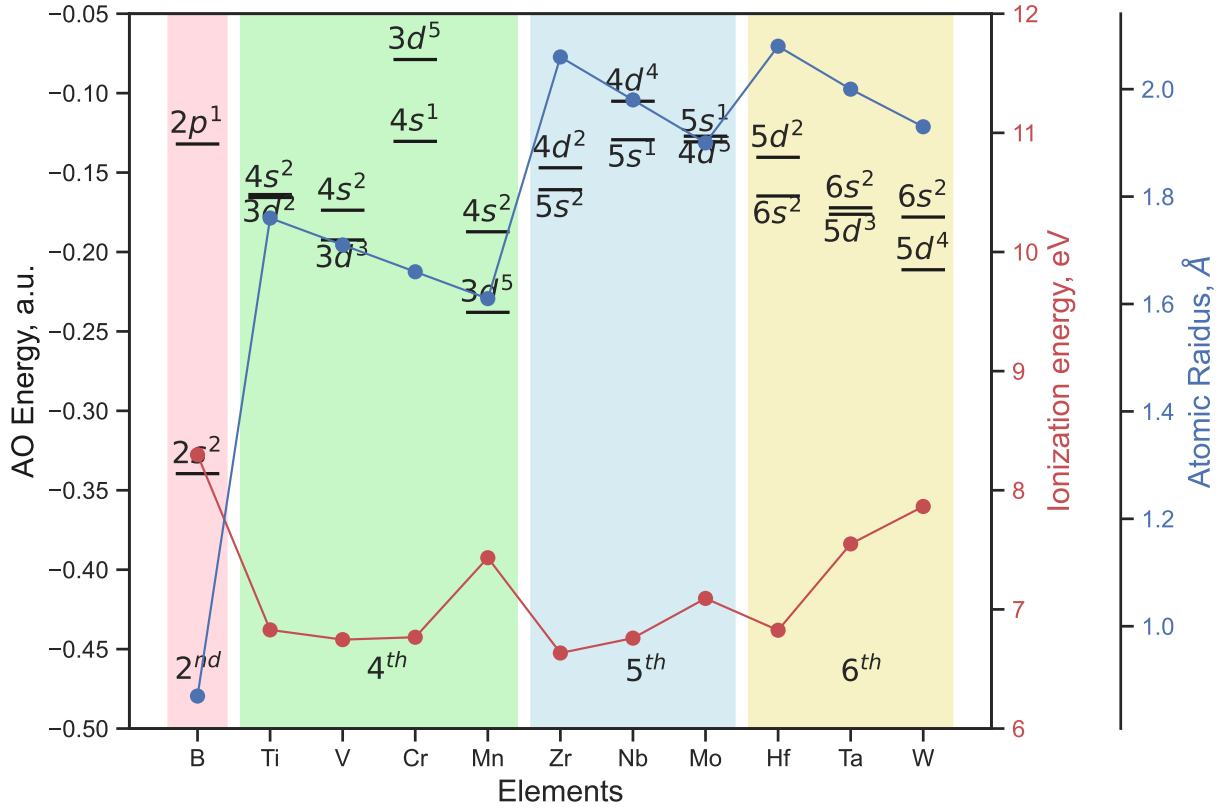

Figure 4.8: Energies of valence AO orbitals [KLS97b, KLS97a, KLS09], 1$^{\text{st}}$ ionization energy [Mar96], and calculated atomic radii [CRR67] of the elements of interest.

A possible explanation of the appearance of the bonds between some impurities and the hexagonal boron layer may be found in the comparison of valence atomic orbitals (AOs) (Fig. 4.8.) The 4$^{\text{th}}$ period elements have generally lower lying valence orbitals, especially, 3*d*, which can be significantly lower than B's 2*p* (except for Cr). They are also small atoms, presumably differing in the bonding overlap with the boron. As a result, the elements in the 4$^{\text{th}}$ period form poor bonds with both B_{hex} and $B_{cluster}$ atoms. They act primarily as a means

to reduce the interlayer bond distance and allow B_3 clusters bind better with B_{hex} layer. This explains the reduction in the B_3 Bader charge and stronger B_{hex}−$B_{cluster}$ bonds. The 5th and 6th period elements, on the other hand, bind better to both the clusters and the hexagonal boron layers, with hexagonal layer bonding being more preferable, regardless of the position of the impurity. The simultaneous weakening of B_{hex}−$B_{cluster}$ can be a product of increased separation and the slight π-back donation onto metal's d orbitals.

Therefore, we propose two intrinsic hardening mechanisms for the tetraboride, based on different types of impurities. The 4th period elements enhance the B_{hex}−$B_{cluster}$ bonding by bringing B_{hex} layers closer together, and in this way stiffening the main slip system in the material. This effect is most noticeable in when M occupies the *edge* position—closest to the B_3 cluster. However, it does little in the *middle* position, where the local distortion is far from B_3. We can hypothesize that the effect might eventually lead to favoring the *edge* placement of the impurity with respect to the clusters during synthesis, and/or affect the concentrations of the boron clusters in the doped structure (i.e. the level of the stoichiometric excess of boron). The 5th and 6th period elements bind well to the boron hexagonal layers, forming stronger bonds with the layers than does W itself. This effect can be substantiated by the COHP analysis (Fig. 4.9.)

To further illustrate the mechanism, we calculated the COHP and ICOHP, for the binding to the boron layer for the two impurities that represent the two proposed intrinsic hardening mechanisms (Mn and Hf) (Fig. 4.9). We compare the COHP and ICOHP of the B_{hex}−M bond for the pure model structure, and Hf and Mn *middle*-doped structures. The reason we picked this doping position here is to see the effect in isolation from the possible interactions of the impurity with the boron cluster. We can see that low lying Mn s and d orbitals, its smaller size, and its greater number of d-electrons do not favor the the bonding with the boron layer, featuring the population of the anti-bonding states (seen below the Fermi energy). The B_{hex}−Mn bond is thus the weakest of the three considered in the Figure. On the other hand, Hf (higher d-AO, fewer d-electrons, and lager size) forms a significantly stronger bond with the boron layer, with a major bonding character seen below the Fermi level, and all of the anti-bonding states appearing above the Fermi level. Since some bonding states

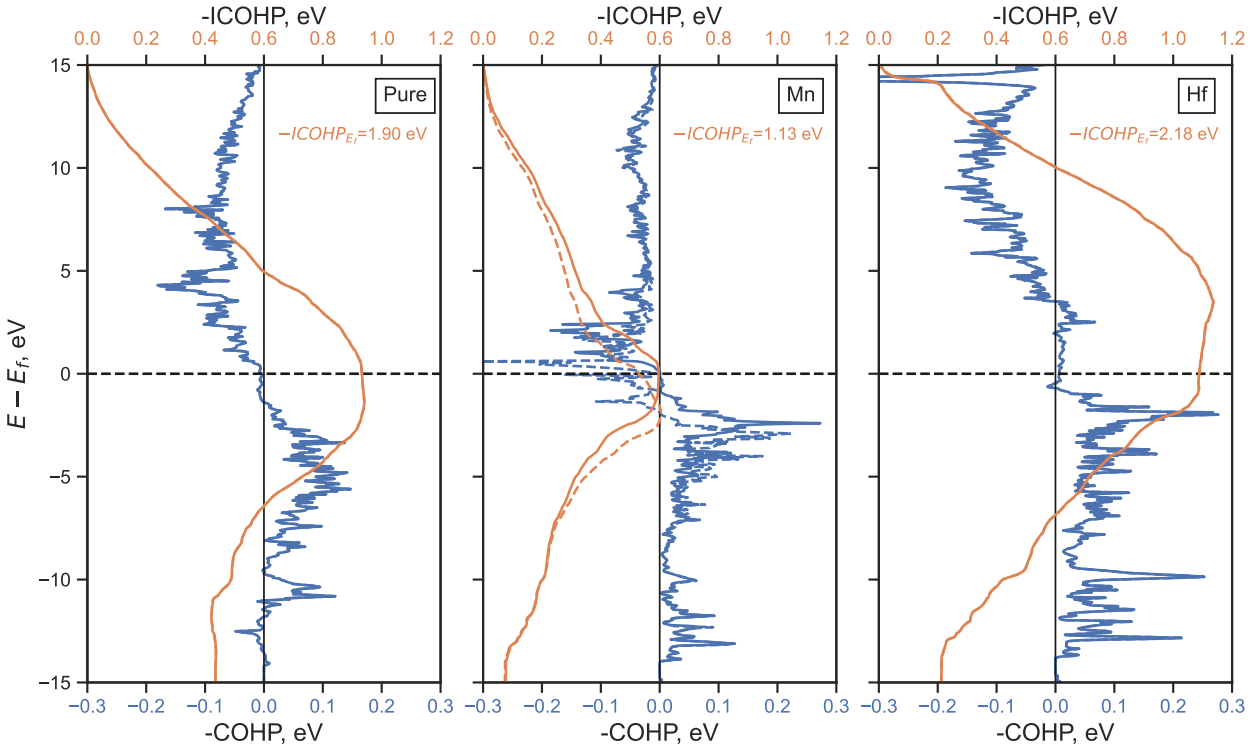

Figure 4.9: COHP and ICOHP of B_{hex}−M (B_{hex}−W for pure structure): ("Pure")—pure structure, ("Mn")—*middle*-doped with Mn, ("Hf")—*middle*-doped with Hf. For all graphs, blue curve corresponds to –COHP, with axis on the bottom, and orange—to ICOHP with axis on the top.

appear above the Fermi level in this case, the material could be made stronger if a chemical mechanism could be found to donate slightly more electrons into this bond.

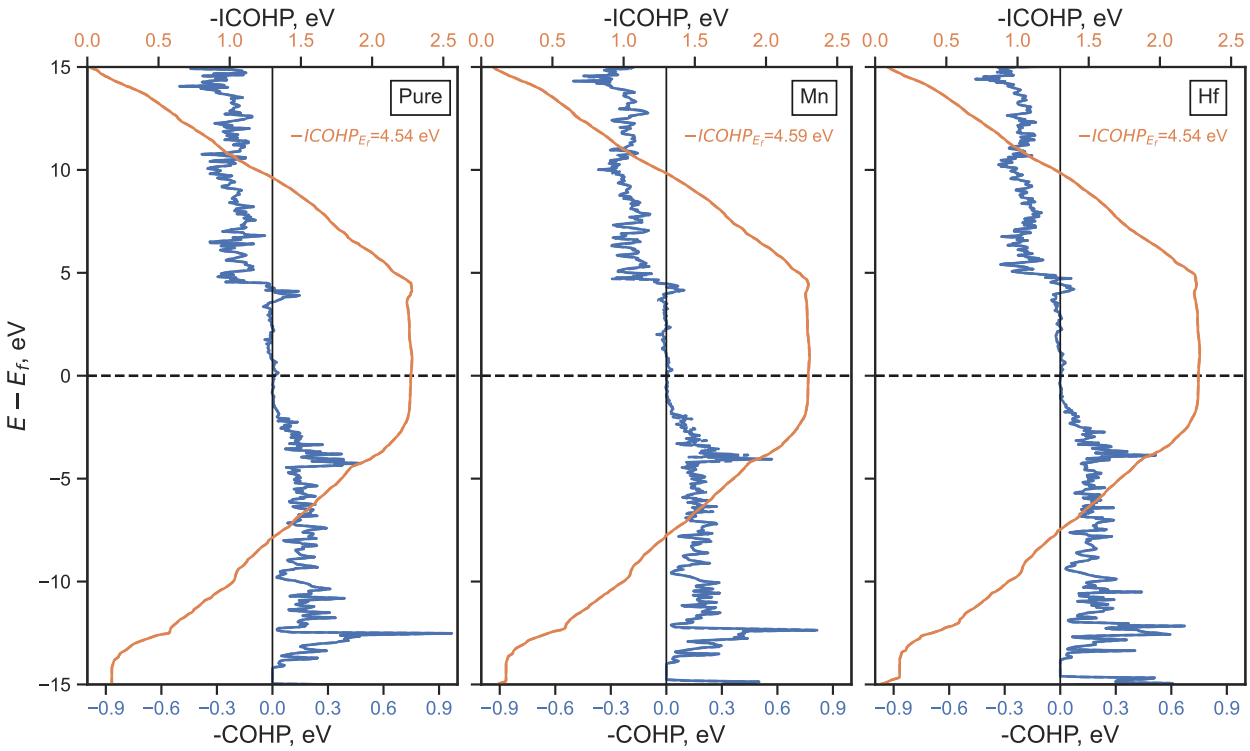

Figure 4.10: COHP and ICOHP of B_{hex}−$B_{cluster}$: ("Pure")—pure structure, ("Mn")—*edge*-doped with Mn, ("Hf")—*edge*-doped with Hf. For all graphs, blue curve corresponds to –COHP (axis at the bottom), and orange—to ICOHP (axis at the top).

The COHP and ICOHP for the B_{hex}−$B_{cluster}$ bond are compared in Fig. 4.10 for the pure model, and the Hf and Mn *edge*-doped structures. In this case, the placement of the impurity is chosen such that the effect on the cluster-layer bonding is most pronounced. All three graphs look very similar, indicating that the impurities do not dramatically affect the nature of the B_{hex}−$B_{cluster}$ bonding, i.e. do not pump or remove electrons from this bonding region. Instead, yet again, the effect of the impurities boils down to affecting the quality of the covalent overlap via changing the bond length, or inter-layer distance, through the size of the impurity. Finally, Fig. 4.11, depicts COHP and ICOHP for the $B_{cluster}$−M bond comparing the pure model, and the Hf and Mn *edge*-doped structures. The placement of impurity in this Figure is the same as in Fig. 4.10. This bond is very weak for all structures, and does

not constitute a major effect in the materials.

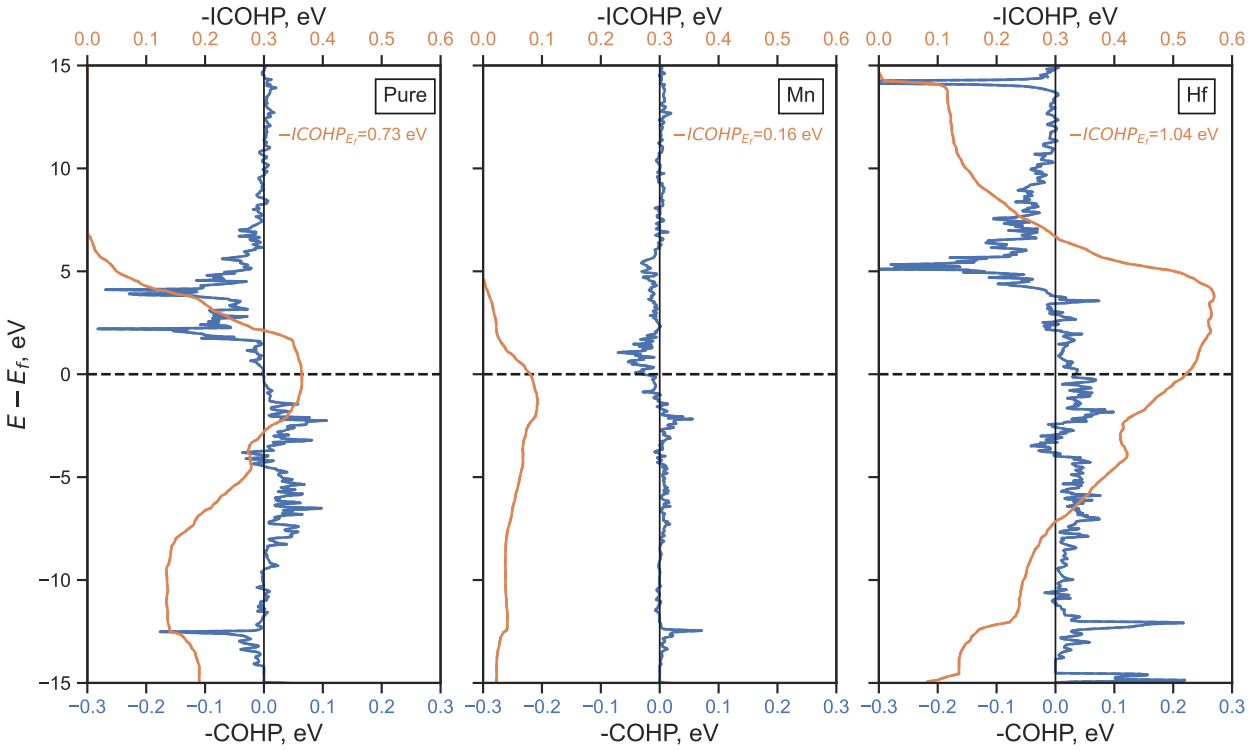

Figure 4.11: COHP and ICOHP of $B_{cluster}$−M ($B_{cluster}$−W for pure structure): ("Pure")—pure structure, ("Mn")—*edge*-doped with Mn, ("Hf")—*edge*-doped with Hf. For all graphs, the blue curves correspond to –COHP (axis at the bottom), and the orange—to ICOHP (axis at the top). Dotted and solid lines are associated with different spins.

We note that, in metallurgy literature, the hardening effect of impurities is most typically attributed to structure locking upon slip to the impurity atom size mismatch. However, here, it is evident that the impurity also affects the bonding within the material. While the impurities affect the boron-boron inter-layer bonding to a small degree, the ability of the impurity itself to bind to the boron layers is a more dramatic effect, and we anticipate it to be important for the mechanical properties of the doped materials. From that point of view, an "ideal" dopant would be smaller than W to enhance the cluster-layer boron-boron bonding, yet itself binding to the boron more strongly than W. If the two bonding effects (metal-layer and cluster-layer bonding) work against each other for a particular impurity, their compounded effect on material's hardness will depend on the stoichiometry (to be studied

in the future). Our results might also imply that the anisotropic compression of the parent tetraboride along the c axis might strengthen the material against slip, as the boron-boron bonding would be made stronger.

4.3 Conclusion

In this work, we studied the doping of the $WB_{4.2}$ boride with transition metals, and elucidated the electronic effects associated with this doping, in relation to material's hardness. We identified substitutional doping in place of W atoms as strongly preferred over occupying the voids in the structure, for all impurities.

Two major substitutional intrinsic hardening mechanisms were found in doped $WB_{4.2}$. The first mechanism is associated with *small radius elements* (4^{th} period elements, such as Ti, V, Cr, and Mn), with low energy $3d$ and $4s$ valence orbitals and smaller size. These elements bind poorly to the boron, both in the B_3 clusters and in the B_{hex} layers, but due to their small size allow the boron hexagonal layers to come closer. Smaller inter-layer distance allows for the stronger B_{hex}−B_{cluster} bonding, increasing hardness. This small-size effect is the strongest when the impurity is closest to the B_3 cluster. The second mechanism is associated with *large radius elements* (5^{th} and 6^{th} period elements), with high-energy nd and $(\text{n}+1)s$ valence orbitals. Large radius elements bind strongly to the hexagonal boron layers and also form weaker bonds to the B_3 clusters. Despite slight weakening of the B_{hex}−B_{cluster} bonds due to increased inter-layer separation in the material, large impurities form strong B_{hex}−M bonds, likely responsible for the enhanced intrinsic hardness. Large-size effect is the strongest when the impurity is farthest from the B_3 cluster, such that the B_{cluster}−M bonding is minimal, B_{hex}−B_{cluster} bonding is intact, and the B_{hex}−M bonding is maximal.

Importantly, despite B_{hex}−B_{cluster} being the strongest inter-layer bond in the material, stronger than any B_{hex}−M or B_{hex}−W bonds, the increase in B_{hex}−M bond strength for large impurities is roughly an order or magnitude greater than the increase in B_{hex}−B_{cluster} bond strength for small impurities. Hence, B_{hex}−M bonding is not to be ignored. Further studies are needed to assess these effects in the context of larger and more realistic unit cells, and

varying placements and concentrations of the boron clusters and the impurities.

REFERENCES

[APM18] Georgiy Akopov, Lisa E. Pangilinan, Reza Mohammadi, and Richard B. Kaner. "Perspective: Superhard metal borides: A look forward." *APL Mater.*, **6**(7), 2018.

[ARS18] Georgiy Akopov, Inwhan Roh, Zachary C. Sobell, Michael T. Yeung, and Richard B. Kaner. "Investigation of ternary metal dodecaborides $(M_1M_2M_3)B_{12}$ (M_1, M_2 and M_3 = Zr, Y, Hf and Gd)." *Dalt. Trans.*, **47**(19):6683–6691, 2018.

[ASY16] Georgiy Akopov, Zachary C. Sobell, Michael T. Yeung, and Richard B. Kaner. "Stabilization of LnB_{12} (Ln = Gd, Sm, Nd, and Pr) in $Zr_{1-x}Ln_xB_{12}$ under Ambient Pressure." *Inorg. Chem.*, **55**(23):12419–12426, 2016.

[AYK17] Georgiy Akopov, Michael T. Yeung, and Richard B. Kaner. "Rediscovering the Crystal Chemistry of Borides." *Adv. Mater.*, **29**(21):1604506, June 2017.

[AYR18] Georgiy Akopov, Michael T. Yeung, Inwhan Roh, Zachary C. Sobell, Hang Yin, Wai H. Mak, Saeed I. Khan, and Richard B. Kaner. "Effects of Dodecaboride-Forming Metals on the Properties of Superhard Tungsten Tetraboride." *Chem. Mater.*, **30**(10):3559–3570, 2018.

[AYT16] Georgiy Akopov, Michael T. Yeung, Christopher L. Turner, Reza Mohammadi, and Richard B. Kaner. "Extrinsic Hardening of Superhard Tungsten Tetraboride Alloys with Group 4 Transition Metals." *J. Am. Chem. Soc.*, **138**(17):5714–5721, May 2016.

[CRR67] E. Clementi, D. L. Raimondi, and W. P. Reinhardt. "Atomic Screening Constants from SCF Functions. II. Atoms with 37 to 86 Electrons." *J. Chem. Phys.*, **47**(4):1300–1307, August 1967.

[CWL07a] H.-Y. Chung, M. B. Weinberger, J. B. Levine, R. W. Cumberland, A. Kavner, J.-M. Yang, S. H. Tolbert, and R. B. Kaner. "Response to Comment on "Synthesis of Ultra-Incompressible Superhard Rhenium Diboride at Ambient Pressure"." *Science*, **318**(5856):1550d–1550d, December 2007.

[CWL07b] H.-Y. Chung, M. B. Weinberger, J. B. Levine, A. Kavner, J.-M. Yang, S. H. Tolbert, and R. B. Kaner. "Synthesis of Ultra-Incompressible Superhard Rhenium Diboride at Ambient Pressure." *Science*, **316**(5823):436–439, April 2007.

[DLW19] Juncai Dong, Haijing Li, Jiaou Wang, Zhiying Guo, Jiangwen Liao, Xingyu Hao, Xiaoli Zhang, and Dongliang Chen. "Nonrandomly Distributed Tungsten Vacancies and Interstitial Boron Trimers in Tungsten Tetraboride." *J. Phys. Chem. C*, **123**(48):29314–29323, November 2019.

[DTD11] Volker L. Deringer, Andrei L. Tchougréeff, and Richard Dronskowski. "Crystal Orbital Hamilton Population (COHP) Analysis As Projected from Plane-Wave Basis Sets." *J. Phys. Chem. A*, **115**(21):5461–5466, June 2011.

[GAE10] Stefan Grimme, Jens Antony, Stephan Ehrlich, and Helge Krieg. "A consistent and accurate ab initio parametrization of density functional dispersion correction (DFT-D) for the 94 elements H-Pu." *J. Chem. Phys.*, **132**(15):154104, April 2010.

[GHC07] R. Grau-Crespo, S. Hamad, C. R.A. A Catlow, N. H. De Leeuw, and N H de Leeuw. "Symmetry-adapted configurational modelling of fractional site occupancy in solids." *Journal of Physics: Condensed Matter*, **19**(25):256201, jun 2007.

[GKS08] Qinfen Gu, Günter Krauss, and Walter Steurer. "Transition Metal Borides: Superhard versus Ultra-incompressible." *Adv. Mater.*, **20**(19):3620–3626, October 2008.

[GLS19] Weiguang Gong, Chang Liu, Xianqi Song, Quan Li, Yanming Ma, and Changfeng Chen. "Unravelling the structure and strength of the highest boride of tungstent $WB_{4.2}$." *Phys. Rev. B*, **100**(22):220102, December 2019.

[HSE03] Jochen Heyd, Gustavo E. Scuseria, and Matthias Ernzerhof. "Hybrid functionals based on a screened Coulomb potential." *J. Chem. Phys.*, **118**(18):8207–8215, May 2003.

[HSE06] Jochen Heyd, Gustavo E. Scuseria, and Matthias Ernzerhof. "Erratum: "Hybrid functionals based on a screened Coulomb potential" [J. Chem. Phys. 118, 8207 (2003)]." *J. Chem. Phys.*, **124**(21):219906, June 2006.

[KF96a] G. Kresse and J. Furthmüller. "Efficiency of ab-initio total energy calculations for metals and semiconductors using a plane-wave basis set." *Comput. Mater. Sci.*, **6**(1):15–50, July 1996.

[KF96b] G. Kresse and J. Furthmüller. "Efficient iterative schemes for ab initio total-energy calculations using a plane-wave basis set." *Phys. Rev. B*, **54**(16):11169–11186, October 1996.

[KH93] G. Kresse and J. Hafner. "Ab initio molecular dynamics for liquid metals." *Phys. Rev. B*, **47**(1):558–561, 1993.

[KH94] G. Kresse and J. Hafner. "Ab initio molecular-dynamics simulation of the liquid-metal–amorphous-semiconductor transition in germanium." *Phys. Rev. B*, **49**(20):14251–14269, May 1994.

[KLS97a] Svetlana Kotochigova, Zachary H. Levine, Eric L. Shirley, M. D. Stiles, and Charles W. Clark. "Erratum: Local-density-functional calculations of the energy of atoms [Phys. Rev. A 55 , 191 (1997)]." *Phys. Rev. A*, **56**(6):5191–5192, December 1997.

[KLS97b] Svetlana Kotochigova, Zachary H. Levine, Eric L. Shirley, M. D. Stiles, and Charles W. Clark. "Local-density-functional calculations of the energy of atoms." *Phys. Rev. A*, **55**(1):191–199, January 1997.

[KLS09] Svetlana K Kotochigova, Zachary H. Levine, Eric L. Shirley, Mark D. Stiles, and Charles W. C Clark. "Atomic Reference Data for Electronic Structure Calculations.", 2009.

[KRF20] Alexander G. Kvashnin, Dmitry V. Rybkovskiy, Vladimir P. Filonenko, Vasilii I. Bugakov, Igor P. Zibrov, Vadim V. Brazhkin, Artem R. Oganov, Andrey A. Osiptsov, and Artem Ya Zakirov. "WB_{5-x}: Synthesis, Properties, and Crystal Structure—New Insights into the Long-Debated Compound." *Adv. Sci.*, **7**(16):2000775, August 2020.

[LTM15] Andrew T. Lech, Christopher L. Turner, Reza Mohammadi, Sarah H. Tolbert, and Richard B. Kaner. "Structure of superhard tungsten tetraboride: A missing link between MB_2 and MB_{12} higher borides." *Proc. Natl. Acad. Sci.*, **112**(11):3223–3228, March 2015.

[LWZ19] Ying Long, Zong Wu, Xin Zheng, Hua Tay Lin, and Fenglin Zhang. "Mechanochemical synthesis and annealing of tungsten di- and tetra-boride." *J. Am. Ceram. Soc.*, (August):1–8, 2019.

[LYM19] Jialin Lei, Michael T. Yeung, Reza Mohammadi, Christopher L. Turner, Jinyuan Yan, Richard B. Kaner, and Sarah H. Tolbert. "Understanding the mechanism of hardness enhancement in tantalum-substituted tungsten monoboride solid solutions." *J. Appl. Phys.*, **125**(8):082529, February 2019.

[Mar96] Wiese W. L. Martin W. S. "Atomic Spectroscopy." In Gordon G. W. Drake, editor, *At. Mol. Opt. Phys. Handb.*, chapter 10, pp. 135–153. AIP Press, Woodbury, NY, 1996.

[MDT13] Stefan Maintz, Volker L. Deringer, Andrei L. Tchougréeff, and Richard Dronskowski. "Analytic projection from plane-wave and PAW wavefunctions and application to chemical-bonding analysis in solids." *J. Comput. Chem.*, **34**(29):2557–2567, November 2013.

[MDT16] Stefan Maintz, Volker L. Deringer, Andrei L. Tchougréeff, and Richard Dronskowski. "LOBSTER: A tool to extract chemical bonding from plane-wave based DFT." *J. Comput. Chem.*, **37**(11):1030–1035, 2016.

[MLX11] R. Mohammadi, A. T. Lech, M. Xie, B. E. Weaver, M. T. Yeung, S. H. Tolbert, and R. B. Kaner. "Tungsten tetraboride, an inexpensive superhard material." *Proc. Natl. Acad. Sci.*, **108**(27):10958–10962, July 2011.

[MSZ11] Naihua Miao, Baisheng Sa, Jian Zhou, and Zhimei Sun. "Theoretical investigation on the transition-metal borides with Ta_3B_4-type structure: A class of hard and refractory materials." *Comput. Mater. Sci.*, **50**(4):1559–1566, February 2011.

[MTX16] Reza Mohammadi, Christopher L. Turner, Miao Xie, Michael T. Yeung, Andrew T. Lech, Sarah H. Tolbert, and Richard B. Kaner. "Enhancing the Hardness of Superhard Transition-Metal Borides: Molybdenum-Doped Tungsten Tetraboride." *Chem. Mater.*, **28**(2):632–637, 2016.

[MXL12] Reza Mohammadi, Miao Xie, Andrew T. Lech, Christopher L. Turner, Abby Kavner, Sarah H. Tolbert, and Richard B. Kaner. "Toward Inexpensive Superhard Materials: Tungsten Tetraboride-Based Solid Solutions." *J. Am. Chem. Soc.*, **134**(51):20660–20668, December 2012.

[NEG20] Ryky Nelson, Christina Ertural, Janine George, Volker L. Deringer, Geoffroy Hautier, and Richard Dronskowski. "LOBSTER: Local orbital projections, atomic charges, and chemical-bonding analysis from projector-augmented-wave-based density-functional theory." *J. Comput. Chem.*, **41**(21):1931–1940, 2020.

[PBE96] John P. Perdew, Kieron Burke, and Matthias Ernzerhof. "Generalized Gradient Approximation Made Simple." *Phys. Rev. Lett.*, **77**(18):3865–3868, October 1996.

[PBE97] John P. Perdew, Kieron Burke, and Matthias Ernzerhof. "Errata: Generalized Gradient Approximation Made Simple." *Phys. Rev. Lett.*, **78**(7):1396–1396, February 1997.

[PWL18] Yong Pan, Xiaohong Wang, Songxia Li, Yanqiong Li, and Ming Wen. "DFT prediction of a novel molybdenum tetraboride superhard material." *RSC Adv.*, **8**(32):18008–18015, 2018.

[RBP09] A. Otero-de-la Roza, M.A. Blanco, A. Martín Pendás, and Víctor Luaña. "Critic: a new program for the topological analysis of solid-state electron densities." *Comput. Phys. Commun.*, **180**(1):157–166, January 2009.

[RJL14] A. Otero-de-la Roza, Erin R. Johnson, and Víctor Luaña. "Critic2: A program for real-space analysis of quantum chemical interactions in solids." *Comput. Phys. Commun.*, **185**(3):1007–1018, March 2014.

[RM15] M. Råsander and M. A. Moram. "On the accuracy of commonly used density functional approximations in determining the elastic constants of insulators and semiconductors." *J. Chem. Phys.*, **143**(14):144104, oct 2015.

[TXZ12a] Yongjun Tian, Bo Xu, and Zhisheng Zhao. "Microscopic theory of hardness and design of novel superhard crystals." *Int. J. Refract. Met. Hard Mater.*, **33**:93–106, July 2012.

[TXZ12b] Yongjun Tian, Bo Xu, and Zhisheng Zhao. "Microscopic theory of hardness and design of novel superhard crystals." *Int. J. Refract. Met. Hard Mater.*, **33**(13):93–106, July 2012.

[XMT15] Miao Xie, Reza Mohammadi, Christopher L. Turner, Richard B. Kaner, Abby Kavner, and Sarah H. Tolbert. "Exploring hardness enhancement in superhard tungsten tetraboride-based solid solutions using radial X-ray diffraction." *Appl. Phys. Lett.*, **107**(4):041903, July 2015.

[YLM16] Michael T. Yeung, Jialin Lei, Reza Mohammadi, Christopher L. Turner, Yue Wang, Sarah H. Tolbert, and Richard B. Kaner. "Superhard Monoborides: Hardness

Enhancement through Alloying in $W_{1-x}Ta_xB$." *Adv. Mater.*, **28**(32):6993–6998, August 2016.

[YT11] Min Yu and Dallas R. Trinkle. "Accurate and efficient algorithm for Bader charge integration." *J. Chem. Phys.*, **134**(6):064111, February 2011.

[ZRT18] Guo Xu Zhang, Anthony M. Reilly, Alexandre Tkatchenko, and Matthias Scheffler. "Performance of various density-functional approximations for cohesive properties of 64 bulk solids." *New J. Phys.*, **20**(6), 2018.